atoms

MDPI

Article

Review of the NPA Diagnostic Application at Globus-M/M2

Nikolai N. Bakharev *, Andrey D. Melnik and Fedor V. Chernyshev

Ioffe Institute, St. Petersburg 194021, Russia
* Correspondence: bakharev@mail.ioffe.ru

Abstract: The application of a neutral particle analyzer (NPA) diagnostic at the Globus-M/M2 spherical tokamaks is discussed. Physical principles of the diagnostic are reviewed. Two general approaches—active and passive measurements—are described. Examples of NPA application for the ion temperature and isotope composition measurements are presented. NPA-aided studies of the energetic ions in the MHD-free discharges, as well as in the experiments with sawtooth oscillations and toroidal Alfvén eigenmodes, are considered.

Keywords: neutral particle analyzer; NPA; CX diagnostics; spherical tokamak; ion temperature; isotopic composition; energetic particles

check for updates

Citation: Bakharev, N.N.; Melnik, A.D.; Chernyshev, F.V. Review of the NPA Diagnostic Application at Globus-M/M2. *Atoms* **2023**, *11*, 53. https://doi.org/10.3390/atoms11030053

Academic Editors: Pavel Goncharov, Christian Hill and Kalle Heinola

Received: 9 February 2023
Revised: 2 March 2023
Accepted: 3 March 2023
Published: 7 March 2023

1. Introduction

Neutral particle analyzers (NPAs) are actively used for the ion component study at present tokamaks [1–13] and stellarators [14–18] and will be utilized at ITER [19,20]. The NPA-based diagnostic utilizes analysis of charge-exchange (CX) fluxes of atoms emitted from the plasma. The key feature of this diagnostic, making it stand out from other ion diagnostics and contributing to its widespread application, is the straightforward interpretation of the signal due to the fact that analyzed atoms are former plasma ions, and the energy distribution of these atoms is similar to the one of ions. In addition to this feature, the NPA-based diagnostic possesses high energy and mass resolution and can provide line-integrated or local measurements while operating in passive or active mode, respectively.

Regarding Globus-M, the first NPA was installed at this spherical tokamak in 2001, two years after the first plasma was obtained. Starting from that moment on, the NPA diagnostic was routinely utilized as one of the main tokamak diagnostics, expanded later by the second analyzer. These two NPAs were migrated to Globus-M2 in 2018 and were recently complemented by the third analyzer. At Globus-M/M2 NPAs were used for the study of both thermal and energetic H and D ions in both active and passive modes. It was the only diagnostic providing data on hydrogen decrease in composition, fast ion distribution and, in the experiments without neutral beam injection (NBI), ion temperature. Prior to charge exchange recombination spectroscopy (CXRS) being installed in 2013, NPA was the only diagnostic for ion temperature measurements during NBI heating.

In this paper, the NPA diagnostic application at Globus-M and Globus-M2 spherical tokamaks are reviewed. We discuss such topics as experimental studies of thermal ion distribution, used to determine ion temperature and isotopic composition; the dynamic distribution of the non-Maxwellian fast ion component during the auxiliary plasma heating; and physical principles of the diagnostic, underlying NPA application under consideration. The paper is organized as follows: in Section 2, physical principles of the NPA diagnostic in passive and active mode are discussed; in Section 3, Globus-M/M2 spherical tokamaks, their diagnostics and heating systems are described; in Section 4, ion temperature measurement in passive and active mode is reviewed, followed by the discussion of the isotope composition measurements in Section 5; in Section 6, NPA-related fast ion studies in MHD-free plasma are considered; in Section 7, the influence of the sawtooth oscillations

and Toroidal Alfvén eigenmodes (TAEs) on fast ion distribution, observed using NPA, is shown. Finally, a summary is given in Section 8.

2. Physical Principles

2.1. General Principles

NPA diagnostic is based on the registration and analysis of atomic fluxes emitted by the plasma. In any plasma, in addition to charged particles (electrons and ions), there is a relatively small fraction of residual atoms. In the case of hydrogen plasmas, the main sources of these atoms are penetration of neutral hydrogen from the region outside the plasma; recombination of plasma electrons and ions in the bulk plasma; atomic beams and pellets injected into the plasma; and CX of plasma ions with hydrogen-like impurity ions. The last source plays a significant role in particle energies above 100 keV, so for Globus-M/M2 tokamaks, it can be ignored.

Plasma ions may be neutralized due to CX with the atoms or recombination with electrons. Since, in both cases, momentum transfer by electrons may be neglected, it can be assumed that resulting atoms have the same velocity as ions before neutralization. The reaction rate for ion neutralization in a 6D space (number of atoms born in a space unit volume per unit speed per unit solid angle per second) is described by the relation

$$\Re(v_i, \theta, \varphi_i, \vec{r}) = f_i(v_i, \theta, \varphi, \vec{r}) n_i(\vec{r}) \Big(n_0(\vec{r}) R_{CX}(\vec{v}_i, \vec{r}) + n_e(\vec{r}) R_{rec}(\vec{v}_i, \vec{r}) \Big), \quad (1)$$

where v_i, θ, φ_i are ion speed, polar and azimuthal angles corresponding to velocity $\vec{v}_i$; f_i is velocity distribution (probability to find particle with given velocity per unit speed per unit solid angle) at the point represented by the radius vector $\vec{r}$; n_i is ion concentration; n_0 is atomic concentration; n_e is electron concentration; and R_{CX} and R_{rec} are rate coefficients of CX with atoms and recombination with electrons, respectively, for the ions with velocity $\vec{v}_i$:

$$R_{CX}(\vec{v}_i, \vec{r}) = \int f_0(\vec{v}_0, \vec{r}) \sigma_{CX}(\left|\vec{v}_0 - \vec{v}_i\right|) \left|\vec{v}_0 - \vec{v}_i\right| d^3\vec{v}_0, \quad (2)$$

$$R_{rec}(\vec{v}_i, \vec{r}) = \int f_e(\vec{v}_e, \vec{r}) \sigma_{rec}(\left|\vec{v}_e - \vec{v}_i\right|) \left|\vec{v}_e - \vec{v}_i\right| d^3\vec{v}_e, \quad (3)$$

where $\vec{v}_0$ is atom velocity; $\vec{v}_e$ is electron velocity; and f_0 and f_e are atom and electron velocity distributions, respectively. If there are several atomic species in plasma (for example, hydrogen and deuterium) with different rate coefficients, then the sum of these species should be used in the right part of Formula (1) for the calculation of the total neutralization rate.

Born atoms are not confined by the magnetic field and leave the plasma following the linear motion trajectories. The NPA, located outside the plasma, registers atoms originating along its line of sight (LOS). The rate of particles in a unit velocity interval entering the collimated analyzer is equal to

$$\frac{dN}{dt dv_i} = \Omega S \int_L \Re(v_i, \theta^l, \varphi^l, \vec{r}^l) a(\vec{v}_i^l, l) dl, \quad (4)$$

where integration is carried out along the entire LOS L, and l is coordinated along the LOS; $\vec{r}^l$ is corresponding radius vector; $\vec{v}_i^l$ is velocity directed towards NPA; $\left|\vec{v}_i^l\right| = v_i, \theta^l, \varphi^l$ are polar and azimuthal angles determining this direction; and ΩS is the solid angle parameter determined by the NPA collimator. ΩS is independent of l and represents a solid angle at

which the NPA input aperture can be seen, integrated over the surface $S_\perp$, for which the NPA LOS is a surface normal:

$$\Omega S = \int\limits_{S_\perp} \int\limits_{\Omega_{NPA}} \sin(\theta) d\theta d\varphi dS. \quad (5)$$

In practice, ΩS is determined during calibration, and, as is shown later, this calibration coefficient is not required for many NPA applications, for example, for ion temperature or isotopic composition measurements. The coefficient $a(\vec{v}_i^{\,l}, l)$ takes into account the process of ionization and CX of atoms moving along the NPA LOS. This process leads to the attenuation of the atomic fluxes leaving the plasma. The attenuation coefficient is determined by the following relation:

$$a\left(\vec{v}_i^{\,l}, l\right) = e^{-\int\limits_l^0 \mu(v_0, x) dx}, \quad (6)$$

where 0 corresponds to NPA location; v_0 is atom speed, $v_0 = v_i$; and μ is the linear attenuation coefficient:

$$\mu(v_0, x) = \frac{1}{v_0}(n_i(x) \cdot (R_{CX}(v_0, x) + R_{ii}(v_0, x)) + n_e(x) R_{ei}(v_0, x)), \quad (7)$$

R_{CX}, R_{ii}, and R_{ei} are rate coefficients of CX, ionization by ion impact, and ionization by electron impact, respectively, for the atom with speed v_0.

As a rule, the distribution of neutral particles measured by NPA is described not in velocity but in energy terms. Moreover, in order to exclude the NPA geometry from consideration, the neutral particle flux is normalized to ΩS:

$$\Gamma_{CX}(E_i) \equiv \frac{dN}{dt dE_i} / \Omega S = \int \Re(E_i, \theta^l, \varphi^l, \vec{r}^{\,l}) a(\vec{v}_i^{\,l}, l) dl, \quad (8)$$

where E_i is ion energy, and $\Re(E_i, \theta^l, \varphi^l, \vec{r}^{\,l})$ is the number of atoms born per unit energy per unit solid angle per unit volume per second at the point represented by the radius vector $\vec{r}^{\,l}$.

The fluxes measured by the NPA are integral values. In general, the ion distribution cannot be derived from integral Expressions (4) or (8). Several approaches have been developed to localize measurements. If the fluxes of thermal particles are measured in the plasma with a Maxwellian ion distribution, then with an increase in the energy of the detected particles, their origin will be localized close to the region where the ion temperature is maximum, i.e., to the central region of the plasma. This is caused by the exponential drop in the number of high-energy particles with a decrease in ion temperature. On the contrary, low-energy thermal atoms are born near the plasma boundary, where atomic concentration and, as a consequence, the CX rate are significant. Therefore, it makes it possible to roughly localize measurements of the energy distribution of thermal ions, their temperature, and also the isotope ratio by choosing the energy range of detected CX fluxes. The methodology is described in more detail in Sections 4.1 and 5.

Another approach allowing local measurements is the so-called active diagnostic. The locality is provided by creating a target of atoms with the concentration n_{0t}, which is comparable to or significantly exceeds the background atomic concentration: $n_{0t} \gtrsim n_{0\_bckg}$. At a sufficiently high concentration of the active target, it is possible to achieve the conditions when the neutral flux, generated in the target region, is comparable to or significantly exceeds the remaining passive integral flux along the NPA LOS: $\Gamma^a_{CX} \gtrsim \Gamma^p_{CX}$. The principles and features of the active diagnostic are described in more detail in Section 2.2, with examples given in Sections 4.2 and 6.2.

Another possible approach for NPA data interpretation is the inverse problem solution: ion distribution is reconstructed from a set of experimental measurements, taking into account the sensitivity of signal to different phase space regions (often called weight function) and a priori information. However, the solution to such an ill-posed problem requires extensive regularization, which results in a substitution of the real plasma object with our vision of it. This approach is not discussed in this paper; an example of its application can be found in [21].

It is necessary to notice that for both active and passive measurements, some ion parameters can be estimated by comparing experimental data and modeling. During the modeling process, it is possible to achieve the coincidence of the calculated and measured neutral fluxes by varying the ion-related parameter of interest, for example, central ion temperature. The fitting parameter determined as a result of such a procedure can be considered a local physical value. Examples of such a direct modeling approach are given in Sections 4.2 and 6.2.

2.2. Active Measurements Using Neutral Beam

Interpretation of the NPA data can be facilitated by the application of the active measurement technique. An additional artificial neutral target is created in plasma by a neutral beam (NB), as in the Globus-M/M2 case, or pellet injection. The active part of the signal corresponds to the local 1D speed (or energy) distribution of ions in a phase space since detected atoms are born in the given location (intersection of the NPA LOS and neutral target) with a velocity directed along the NPA LOS.

The active part of the CX flux can be calculated by subtracting the passive signal right after the NBI switch-off from the total signal just before the NBI switch-off. As a rule, for the considered NPA diagnostic in Globus-M/M2, the fraction of the passive signal ranges from a few percent for fast particles to tens of percent for thermal ones. If the finite size of the neutral target can be neglected (e.g., it is small as compared to the plasma size), a local distribution of ions in a 6D phase space can be calculated from (8):

$$F_i(E_i, \theta^t, \varphi^t, \vec{r}^{\,t}) \equiv f_i(E_i, \theta^t, \varphi^t, \vec{r}^{\,t}) n_i(\vec{r}^{\,t}) = \frac{\Gamma^a_{CX}(E_i)}{\langle n_{0t} l \rangle_L R_{CX}(\vec{v}_i^{\,t}, \vec{r}^{\,t}) a(\vec{v}_i^{\,t}, l^t)}, \quad (9)$$

where t corresponds to the neutral target; l_t is the value of l corresponding to the target location; $\theta^t, \varphi^t, \vec{r}^{\,t}$ correspond to $\theta^l, \varphi^l, \vec{r}^{\,l}$ at the intersection of the target and the NPA LOS; $\langle n_{0t} l \rangle_L$ is line integrated target density; and Γ^a_{CX} is an active part of the Γ_{CX}. In the case of NBI application, the neutral target consists of beam b and halo h particles. Thus $\langle n_{0t} l \rangle_L R_{CX}(\vec{v}_i^{\,t}, \vec{r}^{\,t})$ may be calculated using the following expression

$$\langle n_{0t} l \rangle_L R_{CX}(\vec{v}_i^{\,t}, \vec{r}^{\,t}) = \sum_b \int n_{0b} dl \sigma_{CX}(\left|\vec{v}_i^{\,t} - \vec{v}_b\right|) \left|\vec{v}_i^{\,t} - \vec{v}_b\right| + \sum_h \int n_{0h} dl R^h_{CX}(v_i, \vec{r}^{\,t}). \quad (10)$$

Summation in the first term is performed over all beam energy components. In Globus-M/M2 case, the NB injector, based on the positive ion source, has three main energy components, E_{NBI}, $E_{NBI}/2$, $E_{NBI}/3$. Summation in the second term is performed over all halo atom species; $\vec{v}_b$ is beam component velocity.

The Maxwellian-averaged reaction rate coefficient $R^h_{CX}(v_i, \vec{r}^{\,t})$ of ions with speed v_i incident on h-type halo atoms with mass m_h having Maxwellian distribution, characterized by temperature T_h, is calculated as follows:

$$R^h_{CX}(v_i, \vec{r}^{\,t}) = \frac{1}{v_i} \sqrt{\frac{2m_h}{\pi T_h}} \cdot e^{-\frac{m_h v_i^2}{2T_h}} \int_0^\infty v_{ih}^2 \cdot \sigma_{CX}(v_{ih}) \cdot \sinh\left(\frac{m_h v_{ih} v_i}{T_h}\right) \cdot e^{-\frac{m_h v_{ih}^2}{2T_h}} dv_{ih}. \quad (11)$$

Expression (9) allows performing the direct reconstruction of the local value of the ion distribution function at the given location for a certain velocity direction (determined by the NPA geometry) without the solution of the ill-posed inverse problem required in the case of passive measurements. Moreover, it does not require knowledge of the background neutral density profile, which is usually the main source of uncertainty.

3. Experimental Setup

The experimental studies using NPA diagnostic were carried out at the Globus -M [22–24] and Globus-M2 [24–27] spherical tokamaks. These machines have the same vacuum chamber (major radius R = 36 cm, minor radius a = 24 cm) but different electromagnetic systems. At Globus-M, the maximum achievable toroidal magnetic field B_T was 0.5 T, and plasma current I_p did not exceed 250 kA. At Globus-M2, planned B_T and I_p are 1 T and 500 kA, respectively (currently achieved values are 0.9 T and 460 kA).

Globus-M was equipped with two ACORD-type [28] NPAs: ACORD-12 and ACORD-24M. Both analyzers have the same design, shown in Figure 1, but a different number of detectors: 12 and 24, respectively. A flat cleaning capacitor, located in front of the stripping cell, removes charged particles from the particle flux. Atoms are ionized in the stripping cell filled with nitrogen. The secondary ions are subjected to momentum analysis in the field of an electromagnet and mass analysis in the field of an electrostatic deflector (capacitor). Detection of ions is carried out by channel electron multipliers operating in the counting mode. This allows for the provisioning of temporal resolution of particle flux measurements up to 0.1 ms, which is enough to study such fast processes as ion transport due to the majority of plasma instabilities. The NPA range of measured energies (dynamic range is about 7 for both NPAs) and hence corresponding energy of each detector can be adjusted by changing the deflector voltage and electromagnet current. Changing the NPA energy range also allows for obtaining a more detailed energy spectrum by using measurements with different settings in several identical discharges. Note that recently third analyzer (CNPA) [29] was installed at Globus-M2; however, its application was not considered in this work.

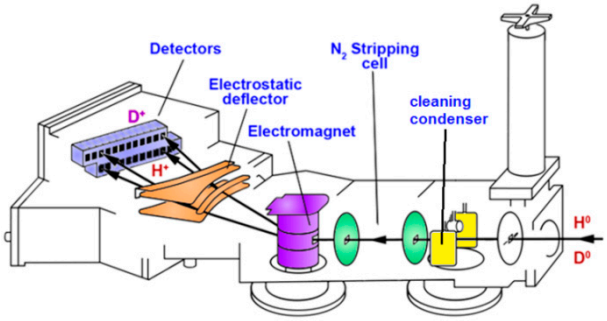

Figure 1. ACORD-type NPA.

The experimental layout, demonstrating the arrangement of NPAs as well as other used diagnostics and heating systems, is shown in Figure 2a. The first NPA ACORD-12 with a transversal line of sight (LOS) has a horizontal scanning angle of 15°, which corresponds to the intersection with NB at R from 32.5 to 40 cm, and a vertical scanning angle of ±10° relative to the equatorial plane (approximately ±17 cm vertical position scan at the intersection with NB). It was used for the ion temperature and isotope composition measurements as well as for the fast ion spectra study during ion cyclotron resonance heating (ICRH). The ACORD-24M NPA has an impact parameter close to the impact parameter of the NB injectors, and its LOS intersects the neutral beam axis at R = 44.6 cm. This analyzer was used for the ion temperature and isotope composition measurements as well as for the fast ion spectra study during NBI. Similar to ACORD-12, scanning systems of the ACORD-24M allows ±10° vertical tilting of the NPA LOS relative to the equatorial plane (approximately ±16 cm vertical position scan at the intersection with NB). Figure 2b

demonstrates the ACORD-24M vertical scanning range, the typical orbit of the fast ion, contributing to the active NPA signal and NB footprint—an area in which the main active signal source is located in the experiments with NBI. NB injector 1, utilized for the active measurements, has an impact parameter of ~32 cm and is equipped with two ion sources (up to 1 MW and up to 500 kW, respectively). It is able to provide 18–30 keV H and D injection. Power distribution along the NB cross section has a 2D Gaussian-like shape: full horizontal width at half maximum (FWHM) is ~1.5 cm, and vertical FWHM is ~20 cm. The second NB injector was not used for the active NPA measurements. It has an impact parameter of ~30 cm and provides 28–50 keV 0.2–1 MW injection. Both injectors are mainly the sources of passing energetic ions. Finally, Globus-M and -M2 were equipped with a 120 kW ICRH heating system, a source of trapped energetic ions.

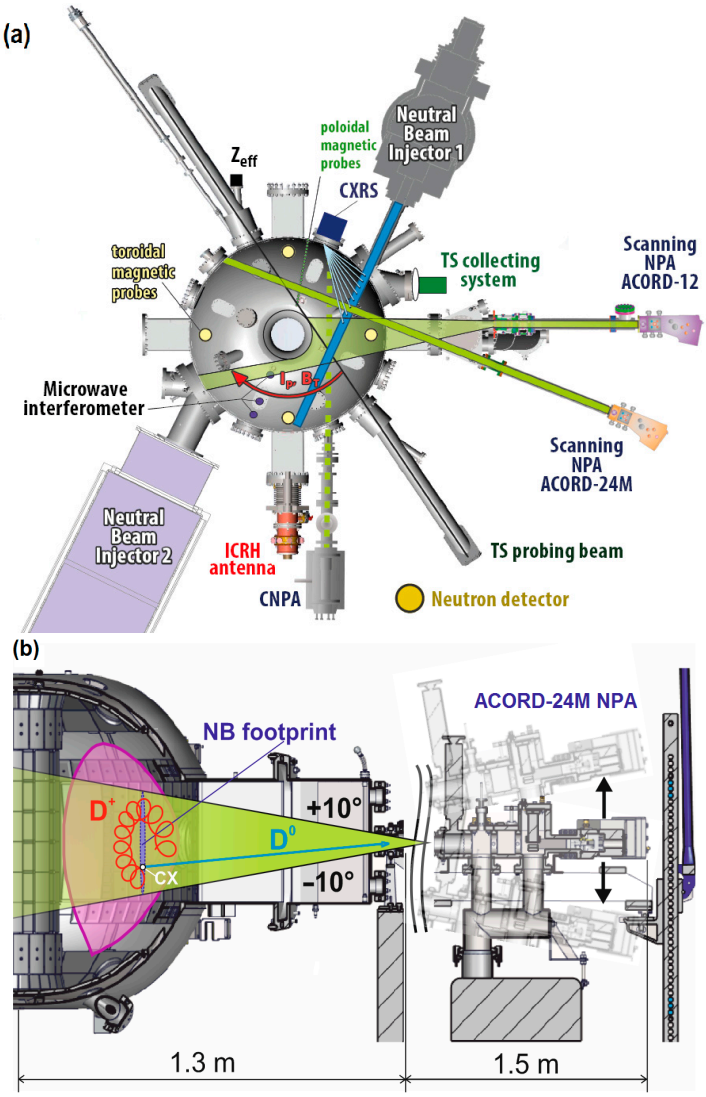

Figure 2. Experimental setup: (**a**) NPA arrangement at Globus-M/M2—top view. (**b**) Illustration of the vertical NPA scanning system. Figure (**b**) is taken from [30]. Reproduced with permission from IOP Publishing.

In addition to the NPA arrangement, Figure 2a shows the layout of other diagnostics essential for the interpretation of the NPA data (the data of these diagnostics are used in Expressions (1)–(4), (6)–(11) or complement the NPA data in the fast ion studies). Electron temperature and density profiles were measured using Thomson scattering (TS) system [31]; the microwave interferometer provided data on a line integrated density evolution; ion

temperature and plasma rotation profiles were obtained using charge exchange recombination spectroscopy (CXRS) system [32,33]; effective charge Zeff was obtained utilizing Zeff diagnostic [34,35]; He^3-filled proportional neutron counter in a polyethylene moderator was utilized for the neutron rate measurement [36]; and fast magnetic probes (frequency range 50–300 kHz) were used for the study of the MHD instabilities. Magnetic configuration was reconstructed using EFIT code [37]. Two codes were applied for the calculation of the fast ion distribution: NUBEAM [38] and a full 3D fast ion tracking algorithm [39], combined with the solution of the Boltzmann kinetic equation [40].

4. Ion Temperature Measurements

The generally accepted assumption used for ion temperature measurements is that plasma ions have an isotropic Maxwellian distribution within the so-called thermal energy range $E < \sim 5T_i$:

$$f_i\left(E_i, \vec{r}\right) \sim \sqrt{E_i} \exp\left(-\frac{E_i}{T_i(\vec{r})}\right). \quad (12)$$

To determine the ion temperature, both passive and active measurements of the CX atom fluxes find an application at Globus-M/M2 tokamaks. Let us consider in more detail each of these methods.

4.1. Passive Measurements

The passive method of ion temperature measurements is applied when the artificially created neutral target in the plasma along the NPA LOS is small or absent. This is either the case without NBI, the case when the active signal is small, or there is no intersection of NPA LOS and the beam atom trajectories. The energy distribution of the detected neutral particle flux Γ_{CX}, similarly to the ion Maxwellian distribution, can be characterized by an effective temperature T_{NPA} which can be obtained from the experimentally measured Γ_{CX} using the following expression:

$$T_{NPA} = -1/\left(\frac{d\ln\left(\frac{\Gamma_{CX}(E_i)}{\sqrt{E_i}}\right)}{dE_i}\right) \quad (13)$$

The example of passive NPA measurement application at Globus-M is presented in Figure 3, where the temporal evolution of the effective ion temperature in the experiments on ion cyclotron plasma heating is shown. Here and below, error bars indicate the standard aleatoric error of each individual measurement unless otherwise stated. The behavior of the temperature in the reference Ohmic discharge was also obtained by the passive method.

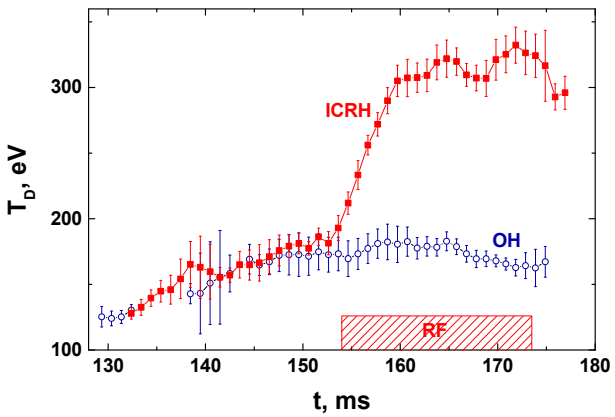

Figure 3. Time evolution of the effective ion temperature measured with NPA in the ICRH experiment and during Ohmic discharges (discharges ##11360–11363). ICRH pulse time is shown by the shaded area. The figure is taken from [41] and reproduced with permission from Springer Nature.

The main question that usually arises in such measurements is whether the effective temperature, estimated using a passive method, corresponds to the central plasma region since the value of central ion temperature is usually the parameter of interest in the analysis of experimental data.

For the Globus-M/M2 tokamaks, we used the traditional approach to obtain information about ions located in the central region of the plasma. Following the common practice, we assumed that low-energy particles in CX flux are primarily related to the peripheral plasma. When estimating the ion temperature, these low-energy particles are excluded from consideration. Only the particles with energies above three central ion temperatures $T_i(\vec{r}^{\,0})$, where $\vec{r}^{\,0}$ corresponds to the magnetic axis coordinate, are taken into account since they are born predominantly in the hot central region of the plasma. In addition, the process of recombination as a source of neutrals is considered to be insignificant. This leads to the simplification of Expression (8) by neglecting the recombination term:

$$\Gamma^0_{CX}(E_i) = \frac{1}{4\pi} n_i(\vec{r}^{\,0}) n_0(\vec{r}^{\,0}) f_i(E_i, \vec{r}^{\,0}) R_{CX}(v_i, \vec{r}^{\,0}) a(\vec{v}^{\,l}_i, \vec{r}^{\,0}) \Delta L, \tag{14}$$

where $n_i(\vec{r}^{\,0})$ and $n_0(\vec{r}^{\,0})$ is the density of ions and atoms in the center of the plasma, respectively; ΔL is the characteristic size of the central plasma region; $f_i(E_i, \vec{r}^{\,0})$ is energy ion distribution in the plasma center; and CX rate coefficient R_{CX} is given by (2) and can be calculated using (11). Then ion temperature can be estimated using iterative direct modeling; $T_i(\vec{r}^{\,0})$ is varied until the experimentally measured $\Gamma^0_{CX}(E_i)$ coincides with the calculated one using the Expression (14).

As an alternative to this approach, a simpler and more demonstrative technique may be implemented [9]. The effective temperature (13) usually differs from the real temperature by no more than tens of percent but does not coincide with it because of the dependence of R_{CX} and a on particle energy. In the case of the local measurements the relation between T_i and T_{NPA} can be represented in the following form:

$$T_i(\vec{r}) = \frac{T_{NPA}}{1 - k_{CX} T_{NPA} + k_\mu(\vec{r}) T_{NPA}}, \tag{15}$$

where k_{CX} and k_μ are coefficients related to the dependence of the CX and attenuation rates on energy, which can be found in [9]. In the case of passive measurements from the plasma center $\vec{r} = \vec{r}^{\,0}$, the dependence of R_{CX} on the ion energy, represented by k_{CX}, causes T_{NPA} to be lower than the actual local ion temperature. This effect is significant only for temperatures higher than several keVs. The dependence of attenuation on atom energy, represented by k_μ, on the contrary, causes T_{NPA} to be higher than the actual ion temperature since atoms with higher energies have a lower probability of being lost on the way from their birthplace to the NPA. For the Globus-M/M2 conditions, the second effect prevails ($k_\mu > k_{CX}$), which means that the effective ion temperature should be higher than the actual central ion temperature. However, in practice, during passive measurements, ΔL is usually relatively large, so outgoing flux is averaged over a significant plasma volume, and effective ion temperature is lower than the central one.

These approaches for central ion temperature estimates are applicable only for low-density or high-temperature plasmas. For the Globus-M/M2 tokamaks, when the central ion temperature $\lesssim 1$ keV, such an approach can be used at the level of average plasma density not higher than 5×10^{19} m^{-3}. This limitation is associated, as noted above, with the screening effect of the plasma center, which results in a significant attenuation of the outgoing CX fluxes from the plasma center to the periphery. In the discharges with ion temperatures higher than several keVs [42], these methods are applicable in the entire experimental density range up to ~2×10^{20} m^{-3}. In dense plasmas with lower ion temperatures, when the simplifying assumption described above does not work, a computer simulation can be used to correct the ion temperature measured by NPAs. For

this purpose, at Globus-M/M2, instead of iterative calculations using (14), the Monte Carlo code DOUBLE-MC [43] was utilized.

4.2. Active Measurements

The active technique implies subtracting the passive part of the signal from the total signal measured by the NPA. This can be performed by subtracting the signal after NBI is switched off from the signal during NBI. Both approaches for ion temperature reconstruction, described in Section 4.1 for localization of passive ion temperature measurements (expression 15 and iterative direct modeling with DOUBLE-MC), may be applied in the case of active technique as well. The active technique minimizes their drawbacks since measurement localization is rather small (~2 cm) and is well known (intersection of the NPA LOS with neutral beam). Moreover, since ion temperature in the NBI discharges is usually higher than in Ohmic discharges, this technique is applicable even at high plasma densities.

As can be seen from Figure 2a, at Globus-M/M2, the LOSs of both analyzers intersect with the injection line of NB injector 1. At the same time, the intensity of the beam emitted by this injector is quite high. As a result, in most cases, a situation favorable for an active method is realized. In this case, it may be considered that the energy distribution of atoms measured by the analyzers using the active technique corresponds to the distribution of plasma ions at the intersection of the NPA observation line and the beam trajectory, taking account of the dependence of R_{CX} and a on particle energy.

An example of the active and passive NPA signal behavior right after the NB switch-off is shown in Figure 4. Here (#41862–#41866), for neutral flux measurements in several discharges with similar parameters, NPA measurements in different energy regions were used in order to cover the entire energy range. NB injector 1 was used for the active measurements until ~209 ms providing a 28.6 keV D injection, and NB injector 2 was turned on during the entire discharge providing a 31 keV D heating beam. As can be seen from Figure 4a, after the NB injector-1 is switched off, the flux of both fast (31.5 keV) and thermal (1.6 keV) atoms falls from about two to several tens of times due to the transition from active to passive measurement mode. Total measured spectra in active (t = 208 ms) and passive (t = 211 ms) modes, shown in Figure 4b, demonstrate that active signal fraction is significant for all NPA energy channels.

The active technique makes it possible to determine not only a local value of the ion temperature but also to obtain a temperature profile, i.e., temperature distribution along the plasma radius. This possibility is implemented by scanning the analyzer's line of sight in a series of similar discharges.

As noted in Section 3, both analyzers at the Globus-M/M2 tokamaks are capable of scanning. Figure 5 shows the effective ion temperature profile obtained as a result of scanning by the ACORD-12 NPA in a series of five discharges with similar parameters. The figure also demonstrates the profiles reconstructed using Expression (15) and iterative calculations with DOUBLE code based on the effective ion temperature profile. In this figure, ρ is a normalized magnetic coordinate: $\rho = \sqrt{\frac{\psi - \psi_{axis}}{\psi_{LCFS} - \psi_{axis}}}$, where ψ is poloidal magnetic flux, ψ_{axis} is ψ on the magnetic axis and ψ_{LCFS} is ψ at the LCFS. Each point in Figure 5 corresponds to measurements in different discharges with ACORD-12, except for $\rho \approx 0.265$, representing averaged temperature obtained using ACORD-24M with a constant LOS. For comparison, the temperature profile measured using CXRS is also shown. As can be seen from the figure, the effective temperature values measured by the NPA exceed the data given by CXRS by 10–15%. However, the reconstructed values of ion temperature using both approaches (Expression (15) and iterative direct modeling with DOUBLE code) are in good agreement with each other and with CXRS data.

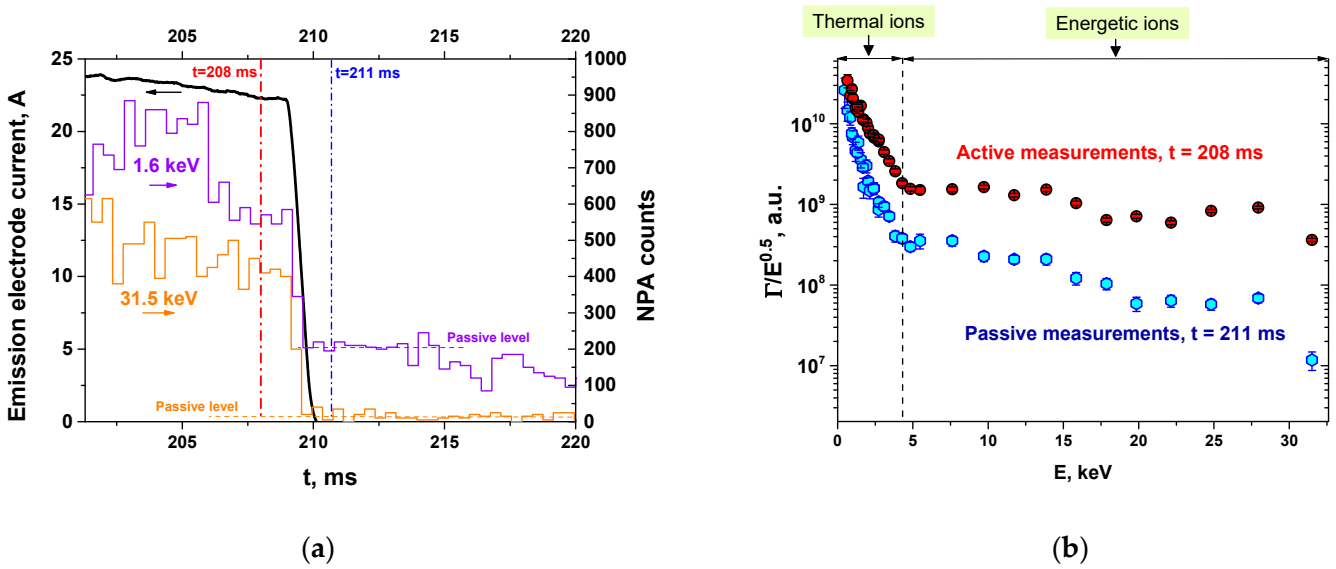

(**a**) (**b**)

Figure 4. Active and passive NPA signals: (**a**) Variation in the NPA count rate after the 28.6 keV NB injector-1 switch off for the case of 1.6 keV (discharge #41866, violet) and 31.5 keV (discharge #41862, orange) atoms. (**b**) NPA spectra obtained before (active, red circles) and after (passive, blue hexagons) NB injector-1 switch off (discharges ##41862–41866 with similar parameters). The moments of measurements correspond to the vertical dash-dotted lines in figure (**a**). Error bars indicate standard error under the assumption that the number of incident atoms is described by the Poisson distribution.

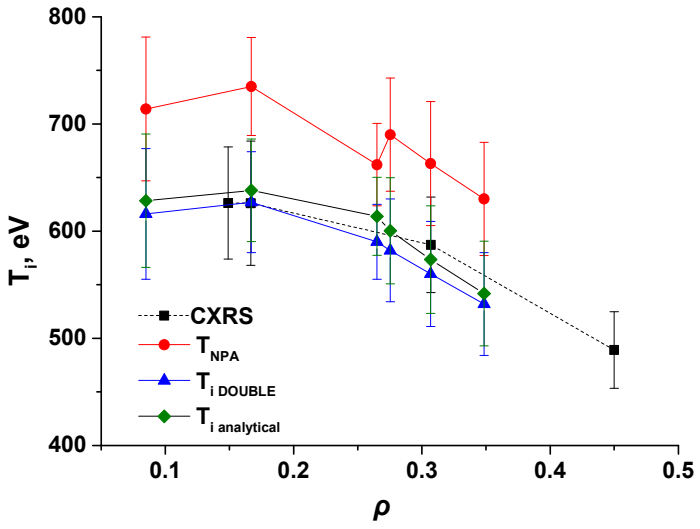

Figure 5. The ion temperature profile in a series of discharges (discharges ##38876,78,79,86,87 with similar parameters) at t = 200 ms. The effective ion temperature profile measured by NPA is shown by circles; the reconstructed ion temperature profiles using the DOUBLE code and semi-analytical Expression (15) are shown by triangles and diamonds, respectively. The CXRS measurement result is shown by black squares. NPA data at $\rho = 0.265$ are obtained with the ACORD-24M NPA, and data at other points are obtained with the scanning ACORD-12 NPA. The figure is taken from [9] and reproduced with permission from IOP Publishing.

5. Isotope Composition Measurements

Isotope composition measurement using NPA is based on the comparison of atomic fluxes of hydrogen isotopes emitted from the plasma. At the Globus-M/M2 tokamaks, such measurements are used to determine the composition of hydrogen–deuterium plasma

using the assumption that both of these isotopes have the same Maxwellian distribution of the form (12) in the thermal energy region. By using the simplifications made in the previous section for low-density plasmas, the isotope ratio in the central region of the plasma can be expressed as:

$$n_H/n_D = \frac{R^D_{CX}(E_i)}{R^H_{CX}(E_i)} \cdot \frac{a^D(E_i)}{a^H(E_i)} \cdot \frac{\Gamma^H_{CX}(E_i)}{\Gamma^D_{CX}(E_i)}, \tag{16}$$

where H and D denotes hydrogen and deuterium, respectively.

As was shown in [44] for small-size plasma devices, the coefficient $\frac{R^D_{CX}(E_i)}{R^H_{CX}(E_i)} \cdot \frac{a^D(E_i)}{a^H(E_i)}$ has a weak dependence on energy. Calculations performed using the DOUBLE code for H-D plasma with the parameters of the Globus-M tokamak showed that in the energy range E = (0.2–2) keV, this coefficient can be considered constant within 10% and equal to 0.70. This allows writing the ratio for the density of H and D in the following simple form:

$$n_H/n_D \approx 0.7 \frac{\Gamma^H_{CX}(E_i)}{\Gamma^D_{CX}(E_i)}. \tag{17}$$

Formula (17) establishes a direct relationship between the density ratio of H and D and the ratio of the corresponding atomic fluxes and makes it possible to determine the plasma isotope composition by comparing the corresponding atomic fluxes entering the analyzer. In practice, instead of n_H/n_D ratio, a percentage content of one of the isotopes in relation to the total number of ions is used as a quantitative characteristic of plasma isotope composition. For example, the content of hydrogen in an *H-D* plasma is defined as

$$C_H = 100 \cdot n_H/(n_H + n_D). \tag{18}$$

Figure 6 shows an example of using this characteristic to illustrate that increase in hydrogen content leads to an improvement of ion heating in the experiments on ion-cyclotron heating at the Globus-M tokamak. In these experiments, the measurement of the hydrogen content, as well as the measurement of the ion temperature, was carried out using the ACORD-12 analyzer.

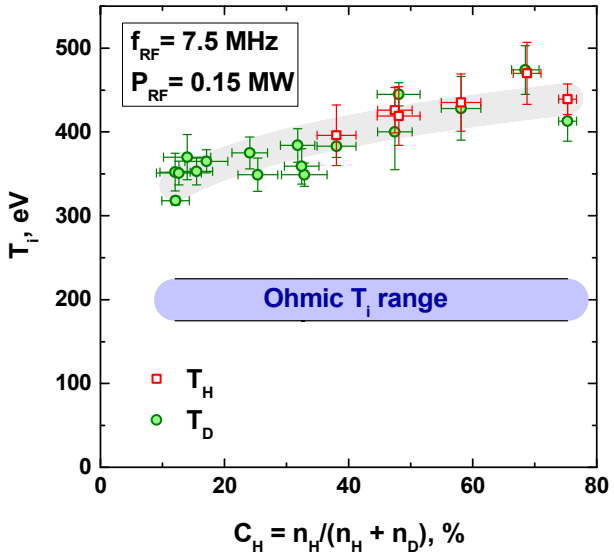

Figure 6. Ion temperature as a function of the H minority concentration in ICRH experiments (discharges ##13773–13801 with different n_H/n_D ratio). Here, T_H and T_D are the temperatures of hydrogen and deuterium ions in an ICRH experiment, and wide blue line is the ion temperature in the Ohmic regime. The figure is taken from [41] and reproduced with permission from Springer Nature.

6. Fast Ion Distribution Measurements

6.1. Passive Measurements

As mentioned above, the fluxes of CX atoms measured in the passive mode are integral characteristics because they come to the NPA from the entire LOS. Despite this fact, passive measurements can be used to obtain general information about plasma ions. As has already been shown, in a number of cases, it is possible to estimate the value of the central ion temperature, as well as to determine the isotopic composition of the plasma. Another possible NPA diagnostic application is the study of the energetic ion behavior. These ions appear during the auxiliary plasma heating, such as ICRH and NBI. As a rule, fast ions are born and confined in the central regions of the Globus-M/M2 plasma. Since their energy significantly exceeds thermal energy, they form the suprathermal "tail" in the energy distribution that can be seen by NPAs. Thus the energy distributions of fast particles can be easily identified in the CX spectrum.

Passive fast ion measurements with NPA were used in the ICRH experiments at Globus-M [41]. Figure 7 shows the CX spectra of hydrogen and deuterium atoms obtained at the ohmic stage of the discharge and during the RF heating. In the experiment, $n_H/(n_H + n_D)$ = 20%. The measurements were performed using the ACORD-12 analyzer, the LOS of which was directed along the major radius of the tokamak. As a result, NPA was capable of recording fluxes of so-called "transverse" particles with pitch angles close to 90°, which are generated during ICRH. The performed measurements confirm the earlier assumption that the main ion heating mechanism was the acceleration of hydrogen minority ions in the ICRH region and the subsequent transfer of their energy to the bulk plasma. This is evidenced by the presence of a characteristic tail of fast ions at energies above 1.5 keV in the hydrogen spectrum but not in the deuterium spectrum, which is visible in Figure 7. This tail is the reason that the difference in H and D fluxes, which is significant in the thermal energy region, vanishes at about 2 keV. The absence of D experimental points above 2 keV is due to poor statistics.

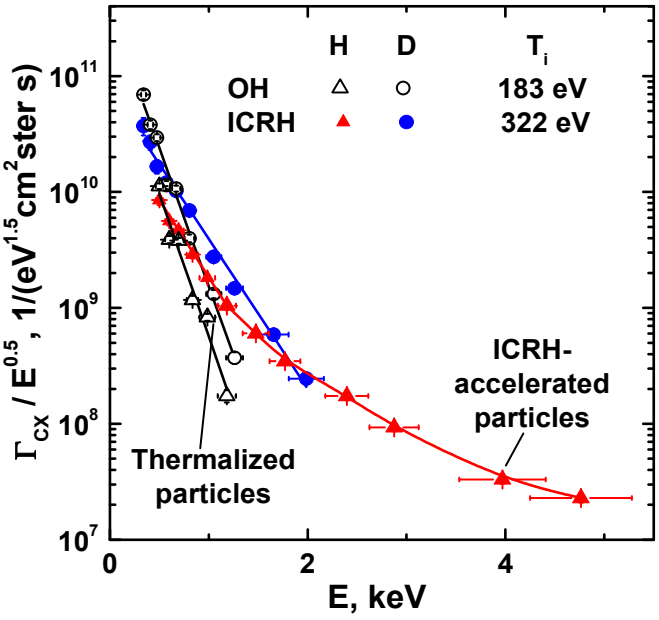

Figure 7. Spectra of CX, H, and D atoms obtained using the ACORD-12 analyzer, which detects "transverse" particles in Ohmic discharge and during ICRH (discharges ##11360–11363). The given value of ion temperature is obtained from D spectrum. The figure is taken from [41] and reproduced with permission from Springer Nature.

6.2. Active Measurements

As it was shown in the previous subsection, the passive measurements of fast CX fluxes can give rough general information about the behavior of suprathermal ions. However, such line-integrated measurements provide only qualitative spatial information, which is often not enough for the study of the spatial fast ion distribution and its evolution. In contrast to this, the active measurements can be used to study the spatially resolved fast ion distribution. Firstly, the unprocessed active NPA signal can be analyzed in order to obtain general information about energetic ion confinement. Figure 8 demonstrates CX atomic spectra measured in active mode with ACORD-24M NPA in shots with different values of I_p and B_T [27]. For clarity, the spectra are normalized in the region of the injection energy. Energies corresponding to the main (E_{NBI}) and secondary ($E_{NBI}/2$, $E_{NBI}/3$, $2E_{NBI}/3$) beam components are specified. One can see a strong U-shaped drop of the atomic fluxes in the region of 15–28 keV and a presence of the so-called "bump-on-tail" in the E_{NBI} region at low values of I_p and B_T, which arises due to the losses of energetic ions during their slowing down. As is shown in Section 7.1, these losses are associated primarily with sawtooth oscillations. The losses are so high that the energy component with 2/3 of the NBI energy, arising due to HD molecule dissociation, is clearly seen, despite the fact that its content in the beam does not exceed several percent. The drop weakens at I_p and B_T increase, and at B_T = 0.8 T and I_p = 0.4 MA, it practically disappears. In this case, the measured spectrum takes a near-classical slowing-down form without a bump-on-tail. Such changes indicate improvement of the fast ion confinement.

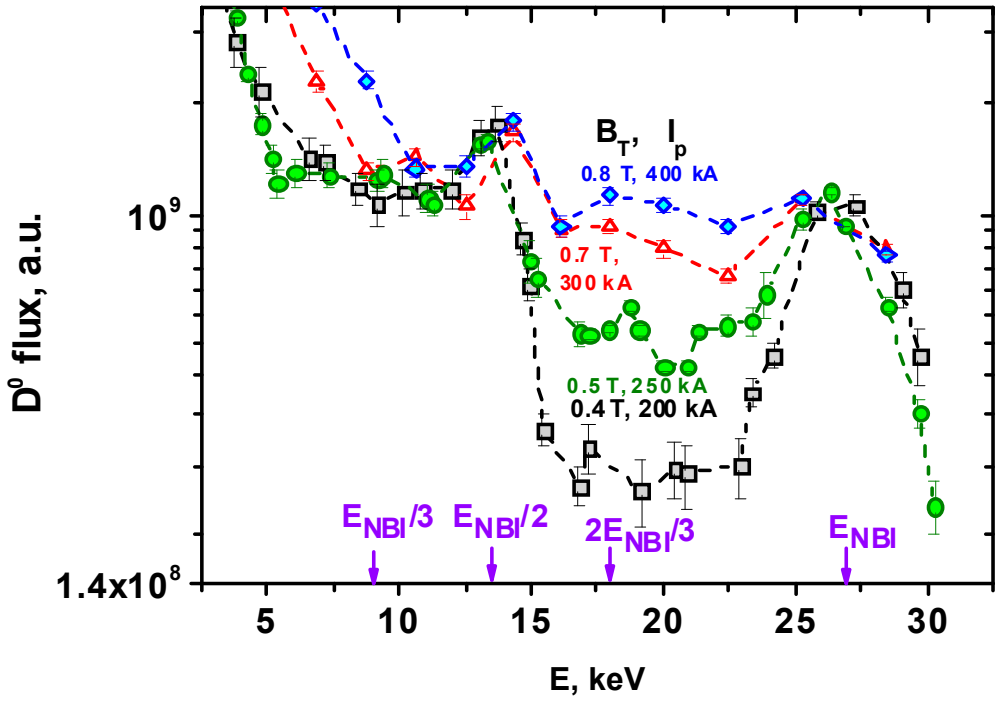

Figure 8. NPA flux, measured in active mode in the discharges with the different B_T and I_p. For clarity, the spectra are normalized in the region of the injection energy. The figure is taken from [27] and reproduced with permission from IOP Publishing.

Direct modeling of the synthetic NPA signal and its comparison with the experimental data is probably the most common approach to the analysis of the experimental data. This approach shows its best side in the case of active measurements. This is due to the fact that the active source of neutrals (in our case, NB) is relatively well known in contrast to the neutral background density. Figure 9 demonstrates energy spectra, measured with ACORD-24M NPA during 18 keV H NBI experiments, and NPA signals, simulated using fast ion distribution calculated with NUBEAM (note that the NUBEAM spectrum does not include

Maxwellian part) and 3D tracking algorithm combined with the solution of the Boltzmann kinetic equation [45]. In order to minimize a discrepancy between measurements and model caused presumably by the uncertainty in the solid angle parameter, the calculated spectra are normalized using the coefficient (~1.3) obtained from a large number of thermal ion measurements in other discharges. As can be seen from the figure, the modeling results are in good agreement with the experiment, demonstrating the adequacy of the fast ion distribution calculation.

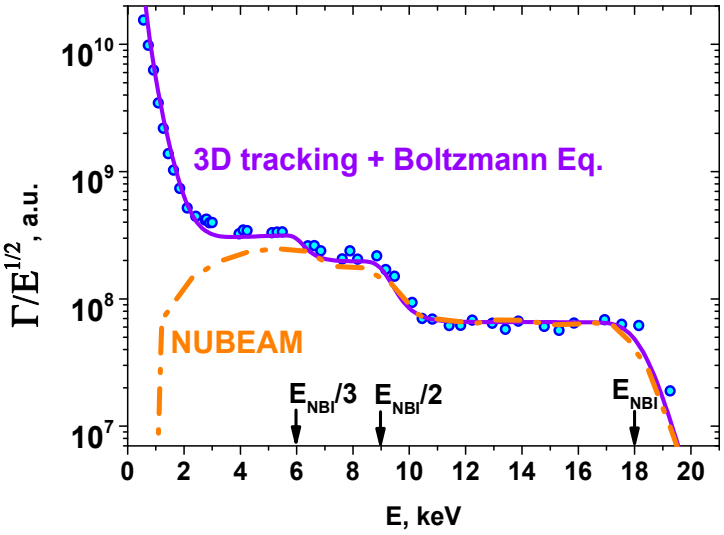

Figure 9. CX spectra measured by NPA (blue dots), discharges ##32990–32998, and simulated ones using fast ion distribution calculated by NUBEAM (orange dash-dot line) and 3D tracking algorithm combined with the solution of the Boltzmann kinetic equation (violet solid line). The figure is taken from [46] and reproduced with permission from IOP Publishing.

Direct modeling can be used in order to estimate one or more unknown fast ion-related parameters. In this case, parameters of interest should be varied in order to minimize differences between the simulated and the experimental NPA spectra. This approach was used to study the influence of I_p and B_T on first orbit losses of energetic ions in Globus-M (here, by first orbit losses, we understand the losses due to collision with tokamak wall as well as the losses due to CX outside of the plasma, which happens in short times, sufficiently smaller than slowing-down time). Direct losses are a sum of shine-through losses when injected atoms leave plasma without being ionized and first orbit losses. Experimental estimates of the first orbit losses were obtained by choosing the source function of the Boltzmann kinetic equation in such a way that the simulated NPA spectrum matches the experimental data. In this case, the difference between chosen and calculated sources corresponds to the first orbit losses. Details of this method can be found in [39]. As an alternative approach, a confined fraction of energetic ions was calculated by means of a 3D tracking algorithm. Shine-through losses are estimated by modeling in both approaches. The results of the calculations and experimental estimations are demonstrated in Figure 10. Both approaches show that in addition to the dependence of first orbit losses on plasma current observed in the conventional and spherical tokamaks, there is a weaker scaling with the magnetic field typical for spherical machines. The reasons for these dependencies are the inner shift of the orbit due to I_p rise and contraction of the orbit width due to the Larmor radius decrease at B_T rise. As a result, as I_p and B_T increase, particle trajectories move away from the wall (so fewer ions are lost due to wall collision) and plasma border (so CX losses decrease due to lower neutral density).

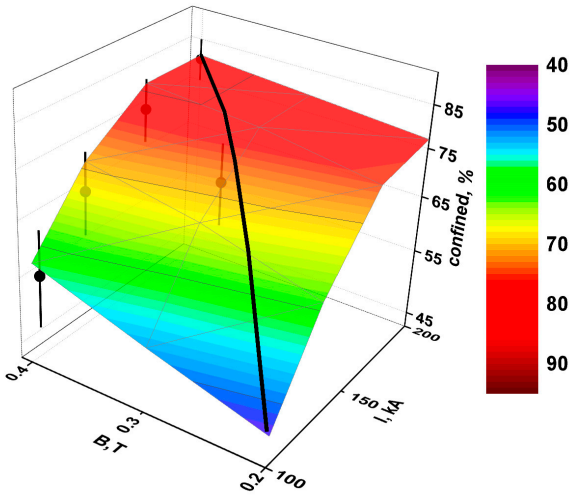

Figure 10. Dependence of the fast ion fraction that has not undergone direct losses on I_p and B_T for the case of 18 keV H NBI. Experimental estimate of the confined fraction is shown by dots. Modeling results are represented by the surface. Black line represents the border of the $I_p/B_T > 500$ kA/T region, where instabilities related to a decrease in safety factor near the plasma boundary occur. The figure is taken from [46] and reproduced with permission from IOP Publishing.

Finally, active NPA measurements allow localization of the experimental fast ion distribution in the phase space. If we neglect the size of the active measurement region (in our case it is the intersection of the NPA LOS with the NBI line), the obtained flux will reflect the energy distribution of the fast ions with the determined velocity direction (towards the NPA) in the measurement region. NPA is the only energetic ion diagnostic allowing such detailed localization. In order to obtain part of the fast particle distribution from the measured atomic flux, Expression (9) should be used. While in general, NB and NPA LOSs have finite dimensions, masking the local features of the fast ion distribution in Globus-M/M2, NB and LOS sizes are small compared to the full measurement range, and the masking effect is minor.

An example of the local fast ion distribution reconstruction is presented in Figure 11a. Note the absolute scale of the given spectrum. Fast ion distribution at the same coordinates and pitch angles as in the experiments was calculated with NUBEAM (Figure 11b). For convenience, energy ion distributions at three different spatial locations are shown in Figure 12. Modeling reproduces the following main trends: (1) a decrease in the fast ion concentration from the center to the LCFS; (2) the existence of three peaks corresponding to three main NBI energy components (E_{NBI}, $E_{NBI}/2$, $E_{NBI}/3$). These peaks are most pronounced in the plasma center, where NB absorption per unit volume is maximal and becomes smoother in the outer plasma region. At the same time, the simulation failed to reproduce the steep concentration drop in the bottom left corner of the figure. Despite the fact that drift approximation in NUBEAM is adapted for use in STs, a part of the information is probably still lost during the conversion from the distribution of the guiding centers used in NUBEAM to the particle distribution. The drop in the distribution is reasonably well explained by the reverse full orbit modeling. The results of this modeling are shown in Figure 11a. The black line presented in this figure separates ions, which circulate inside the plasma, from the ions with orbits intersecting LCFS. The orange line separates confined ions from the ions, hitting the first wall. It can be seen that drop in the fast ion concentration is observed near the plasma boundary. These ions have a high probability of undergoing CX losses in the outer part of their orbits where atomic concentration is high. Energetic ion concentration drop continues to the area where ions begin to hit the wall. The measured fast ion concentration in this region is close to the standard error level.

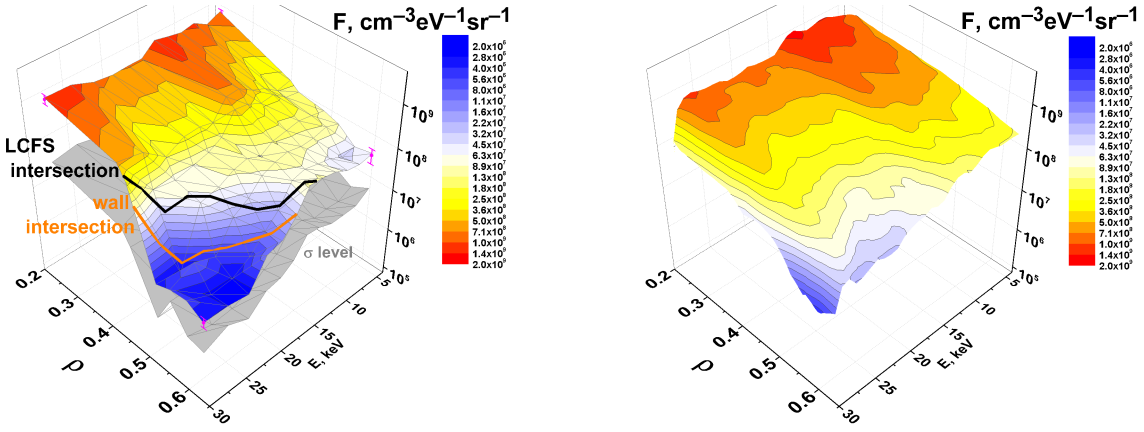

Figure 11. Experimental energy and spatial distribution of the fast deuterium, reconstructed using expression 9 (**a**) (discharges ##39001, 39006-9, 39013, 39015 with similar parameters; energy spectra were measured at different spatial locations from discharge to discharge) and simulated with NUBEAM (**b**). Grey surface shows standard error level. Magenta error bars show epistemic uncertainty. Black and orange lines indicate the borders below which the ion orbits intersect the LFCS and tokamak wall, respectively. The figure is taken from [30] and reproduced with permission from IOP Publishing.

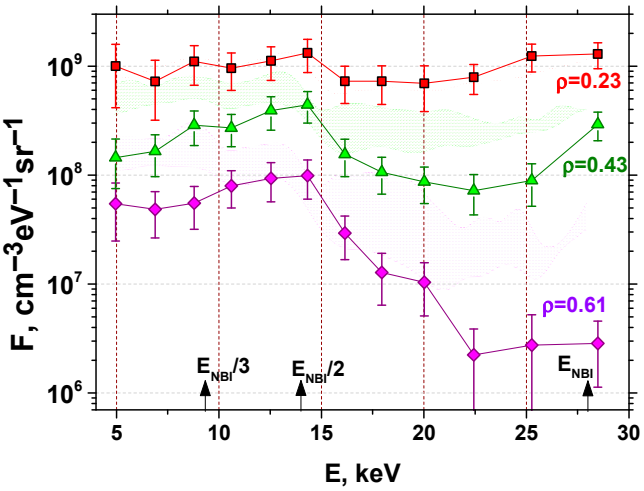

Figure 12. Fast ion energy distribution at different spatial locations obtained in the experiment using active NPA diagnostic (points and lines) and simulated using NUBEAM (filled areas). Error bars—sum of the epistemic and aleatoric (95% confidence interval) errors. The figure is taken from [30] and reproduced with permission from IOP Publishing.

7. Fast Ion Spectra Change during Instabilities

7.1. Sawtooth Oscillations

The effect of sawtooth oscillations on the fast particle confinement was observed at the Globus-M tokamak during NBI with energies of 25–30 keV and power of 600 kW. The experiments were carried out at I_p = 200 kA, B_T = 0.4 T, and an average plasma density of 3.5–4 $\times$ 10^{19} m^{-3}. Typical values of ion and electron temperature were 400–500 eV and 500–600 eV, correspondingly. The CX spectra were measured using the ACORD-24M analyzer. Since the NPA line of sight intersected the NBI line at a major radius R = 0.446 m, it was possible to perform the active measurements of CX fluxes coming from the central region of the plasma.

The behavior of the registered suprathermal particle flux with energy close to the main injection energy is shown in Figure 13. In order to identify the moments of internal reconnection, the figure also includes the signals of a soft X-ray monitor and neutron detector. As can be seen from the figure at the sawtooth crash, the atomic flux drops sharply. The flux decrease during reconnection reaches 90%. In the intervals between drops, the CX flux gradually increases and returns to the initial value. As can be seen from Figure 13, the neutron rate drop is significantly lower than the NPA drop. In the Globus-M tokamak, neutron yield is determined primarily by beam–plasma interaction and hence roughly proportional to the number of fast ions and to the concentration of thermal ions. The difference in the signal of the neutron detector and NPA indicates that fast ions are redistributed from the phase space region observed by NPA, but not all of them are lost. Since the decrease in neutron rate is associated not only with the fast ion losses but also with their transport to the outer region, where thermal ion density is lower and fusion reaction rate has strong energy dependence, the neutron drop (which is 20–30%) may be used only for a rough estimation of fast ion losses.

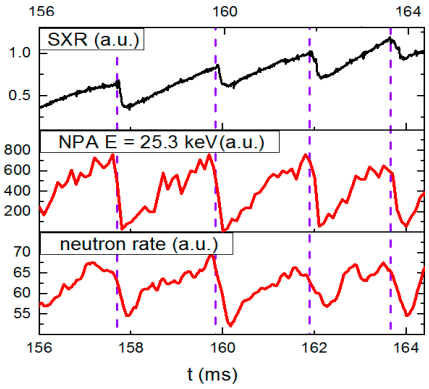

Figure 13. The time traces of signals during sawtooth oscillations in discharge #31965. From top to bottom: soft X-ray, 25.3 keV atomic flux, neutron rate. The figure is taken from [45] and reproduced with permission from IOP Publishing.

The CX spectra recorded before and immediately after the reconnection are shown in Figure 14. After reconnection, the number of particles registered by the analyzer decreases in the whole suprathermal energy range. Both spectra have a noticeable U-shaped drop between E_{NBI} and $E_{NBI}/2$. Such spectra shape can be explained by the losses and redistribution of fast ions over space and pitch angles, which occur at the moments of reconnection.

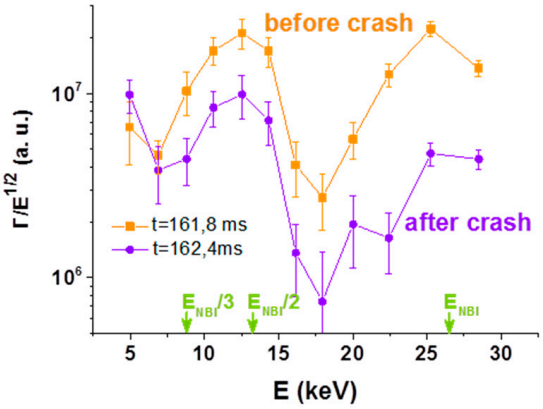

Figure 14. Fast CX atom spectra in discharge #31965 with sawtooth oscillations: squares—before reconnection; circles—after reconnection. The figure is taken from [45] and reproduced with permission from IOP Publishing.

The shape of the spectrum shown in Figure 14 is explained by the following consideration. The period of sawtooth oscillations in the considered experiments is about 2 ms. The characteristic slowing-down time of fast ions is about 10 ms. Particles generated with the injection energy do not have time to slow down considerably and fill the space between the NBI peaks during the time between reconnections. These conditions lead to the formation of the U-shaped drop between E_{NBI} and $E_{NBI}/2$.

7.2. Toroidal Alfvén Eigenmodes

Another example of the NPA application for the instability-induced fast ion transport study is measurements in the discharges with Toroidal Alfvén eigenmodes (TAE). At Globus-M/M2, these instabilities lead to energetic ion redistribution, observed using the active NPA technique. Figure 15 demonstrates a variation in the 27 keV atomic flux (close to E_{NBI}) at TAE bursts. The local source of this active signal corresponds to $\rho \approx 0.2$, which means that energetic ion transport from the plasma center is observed. Figure 16 shows atomic flux spectra before the instability burst and right after it for the case of D injection into D and H plasmas. Change of the spectra in a wide energy range is observed. The highest signal decrease corresponds to the atomic fluxes with energy close to E_{NBI} (up to 75%), while in both cases, the drop in spectra spreads down to energy that corresponds to the Alfvén velocity.

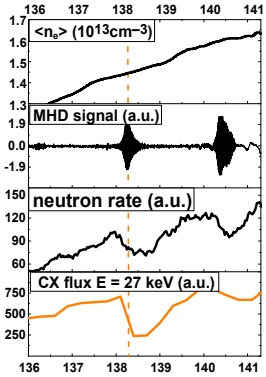

Figure 15. Correlation of neutron rate and CX flux with TAE bursts in discharge #31996. From top to bottom: line-averaged electron density, MHD signal, neutron rate, 27 keV atomic flux. The figure is taken from [45] and reproduced with permission from IOP Publishing.

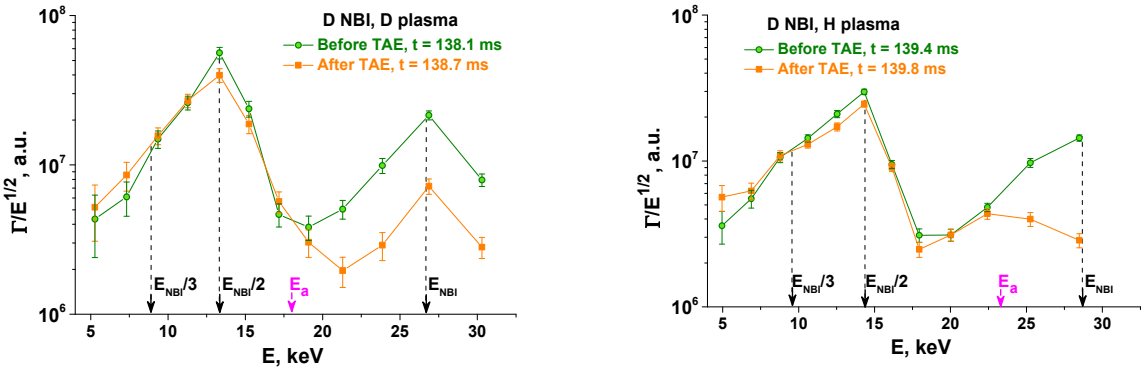

(**a**) (**b**)

Figure 16. CX spectra measured before (green) and after (orange) the TAE burst: (**a**) D injection into D plasma, discharge #31996; (**b**) D injection into H plasma, discharge #31784. E_a—energy corresponding to the Alfvén velocity. Figure (**a**) is taken from [45] and reproduced with permission from IOP Publishing.

Scanning active NPA was utilized for the study of energetic ion spatial transport during TAEs. In the dedicated experimental series (discharges ##39001, 39006-9, 39013, 39015; 800 kW 28.5 keV NBI) vertical NPA scan, similar to the one discussed in Section 6.2, was performed from shot to shot. During the scan, the LOS tilting angle was changed from 0° to -9.3°, which corresponds to ρ change from ~0.23 to ~0.6. Figure 17 demonstrates a variation in the 25.3 keV NPA signals at different NPA positions. In the plasma center, the CX flux drop is observed, indicating ion transport from this region. At $\rho \approx 0.42$, the inversion occurs: the signal stops falling and starts rising during TAE. Such behavior indicates the outward transport of the energetic ions. The closer the investigated region is to the periphery, the faster the signal drops to the pre-TAE level after TAE ends. The reason for such behavior is an increase in CX fast ion losses near the plasma border.

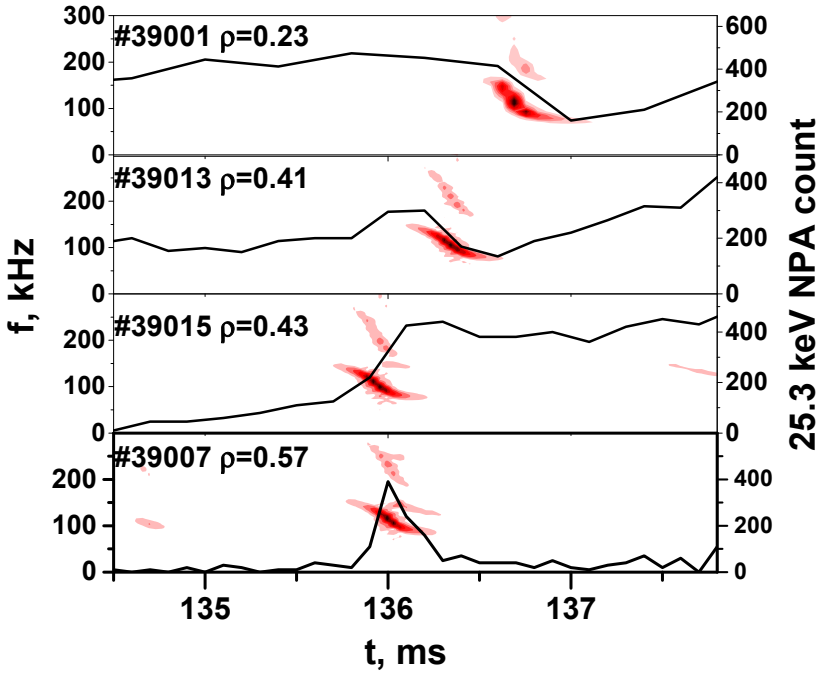

Figure 17. NPA 25.3 ± 1.2 keV atom count rate evolution with TAE development (discharges #39001, 39007, 39013, 39015). Normalized effective radius of the active signal source is increased from top to bottom.

A combination of the two approaches discussed above (measurement of the energy spectrum change and spatial scanning) allows for studying the spatial transport of ions with different energies. Figure 18 shows the reconstructed part of the energy and spatial fast ion distribution before and during TAE using the expression 9. The data were obtained in the dedicated experimental series discussed above (discharges ##39001, 39006-9, 39013, 39015). For convenience, Figure 19 demonstrates a section of Figure 18 at TAE at inner ($\rho \approx 0.23$) and outer ($\rho \approx 0.57$) spatial points. NPA measurements show outward transport in a wide range of energies $E \gtrsim 20$ keV (there is also another region with strong ion transport at $E \approx 11$–14 keV, $\rho \approx 0.45$–0.6, which is not discussed here). As discussed in Section 6.2, the outer region, populated with fast ions during the TAE burst, is characterized by high CX losses. Ions in this region are lost in a short time, so relatively high ion concentration there remains only when instability is active (see lower panels of Figure 17 for example). Thus, it can be argued that TAE leads not only to fast ion transport but also to their losses.

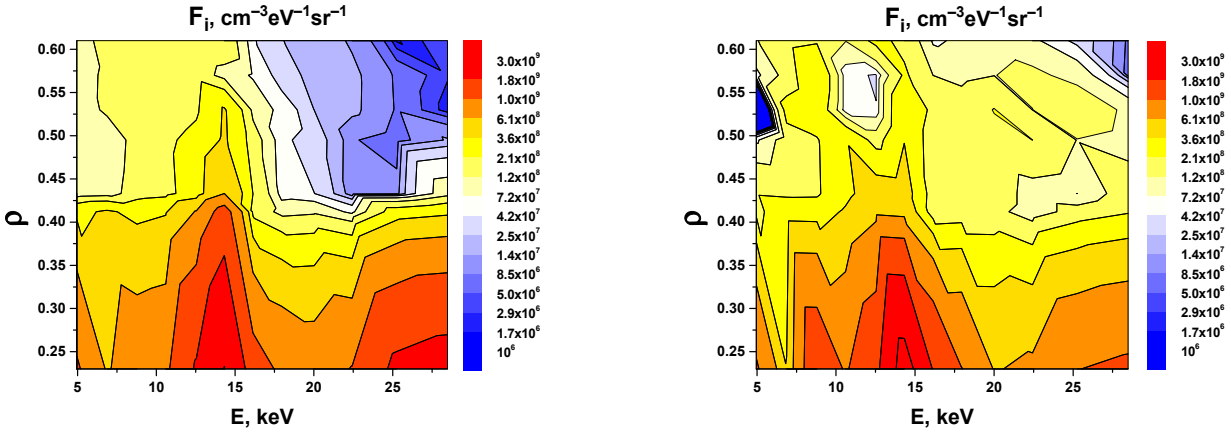

Figure 18. Experimental energy and spatial fast D ion distribution before (**a**) and during (**b**) TAE reconstructed using the active NPA measurements (discharges ##39001, 39006-9, 39013, 39015 with similar parameters; energy spectra were measured at different spatial locations from discharge to discharge).

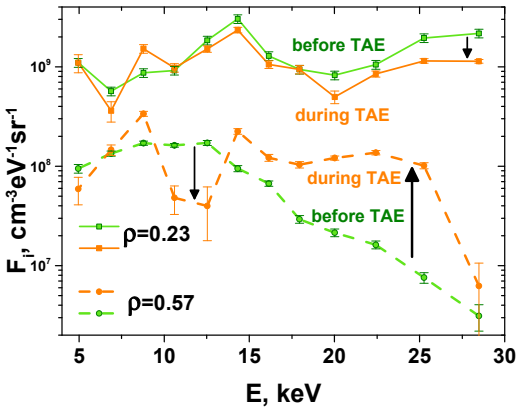

Figure 19. Fast ion energy distribution before and during TAE at inner ($\rho \approx 0.23$, #39002) and outer ($\rho \approx 0.57$, #39007) spatial points, observed by the NPA. Arrows demonstrate direction of change in the fast ion concentration at TAE excitation.

8. Conclusions

Neutral particle analyzers are versatile diagnostic instruments that allow for studying ion components of high-temperature plasma. Since analyzed atoms are former plasma ions, the interpretation of the measured data is straightforward: obtained atomic spectrum reflects the ion distribution adjusted for the dependence of atomic birth rate and neutral flux attenuation on particle energy. As compared to other ion diagnostics, NPA has high energy and mass resolution as well as the ability to conduct line-integrated or local measurements while operating in passive or active mode, respectively.

This paper provides the main physical principles of the diagnostic as well as formulas for the calculation of the NPA signal (Expression (8)) and also for the reconstruction of the plasma parameters from the experimental data: ion temperature (Expressions (13) and (15)), isotopic composition (Expression (16) and (17)), and non-Maxwellian distribution (Expression (9)). NPA capabilities are illustrated with the data obtained at Globus-M/M2 spherical tokamaks. NPAs were used at these machines for more than 20 years in active and passive modes, providing examples for all the discussed diagnostic applications. It was routinely used for the ion temperature and hydrogen ion composition measurements in the pure Ohmic discharges as well as in the discharges with NBI and ICRH heating.

In addition, it provided data on the energetic particle confinement in the ICRH- and NBI-heated plasma. In the active operation mode, it was possible not only to reconstruct local fast ion distribution but also to observe its evolution during instabilities: sawtooth oscillations and toroidal Alfvén eigenmodes.

9. Patents

The work is performed on the Unique Scientific Facility "Spherical tokamak Globus-M", which is incorporated in the Federal Joint Research Center "Material science and characterization in advanced technology".

Author Contributions: Conceptualization, N.N.B. methodology, N.N.B. and F.V.C.; validation, A.D.M. and F.V.C. formal analysis, N.N.B., A.D.M. and F.V.C.; investigation, N.N.B., A.D.M. and F.V.C.; data curation, N.N.B. and F.V.C.; writing—original draft preparation, N.N.B. writing—review and editing, A.D.M. and F.V.C. All authors have read and agreed to the published version of the manuscript.

Funding: Fast ion study at Globus-M2 (Sections 2, 6.2 and 7.2) is supported by RSF research project № 21-72-20007. Thermal ion distribution study (Sections 4 and 5) was performed within the framework of the Ioffe Institute state contract 0034-2021-0001, and tokamak diagnostics preparation (Section 3) was performed in accordance with Ioffe Institute state contract 0040-2019-0023.

Data Availability Statement: Data available on request.

Conflicts of Interest: The authors declare no conflict of interest.

References

1. Karpushov, A.N.; Duval, B.P.; Schlatter, C. Neutral particle analyzer diagnostics on the TCV tokamak. *Rev. Sci. Instrum.* **2006**, *77*, 033504. [CrossRef]
2. Tang, V.; Liptac, J.; Parker, R.R.; Bonoli, P.T.; Fiore, C.L.; Granetz, R.S.; Irby, J.H.; Lin, Y.; Wukitch, S.J.; The Alcator C-Mod Team. Compact multichannel neutral particle analyzer for measurement of energetic charge-exchanged neutrals in Alcator C-Mod. *Rev. Sci. Instrum.* **2006**, *77*, 083501. [CrossRef]
3. Du, X.D.; Van Zeeland, M.A.; Heidbrink, W.W.; Su, D. Development and verification of a novel scintillator-based, imaging neutral particle analyzer in DIII-D tokamak. *Nucl. Fusion* **2018**, *58*, 082006. [CrossRef]
4. Fiore, C.L.; Medley, S.S.; Hammett, G.W.; Kaita, R.; Roquemore, A.L.; Scott, S.D. Ion temperature from tangential charge exchange neutral analysis on the Tokamak Fusion Test Reactor. *Nucl. Fusion* **1998**, *28*, 1315. [CrossRef]
5. Medley, S.S.; Roquemore, A.L. Neutral particle analyzer diagnostic on the National Spherical Torus Experiment. *Rev. Sci. Instrum.* **2004**, *75*, 3625. [CrossRef]
6. Liu, D.; Heidbrink, W.W.; Darrow, D.S.; Roquemore, A.L.; Medley, S.S.; Shinohara, K. Performance of the solid state neutral particle analyzer array on the national spherical torus experiment. *Rev. Sci. Instrum.* **2006**, *77*, 10F113. [CrossRef]
7. Schlatter, C.; Duval, B.P.; Karpushov, A.N. Reconstruction of ion temperature profiles from single chord NPA measurements on the TCV tokamak. *Plasma Phys. Control. Fusion* **2006**, *48*, 1765–1785. [CrossRef]
8. Boivin, R.L.; Koltonyuk, M.; Munson, C.P.; Mayo, R.M. Time-of-flight neutral particle analyzer for Alcator C-Mod. *Rev. Sci. Instrum.* **1997**, *68*, 982. [CrossRef]
9. Bakharev, N.N.; Chernyshev, F.V.; Gusev, V.K.; Kiselev, E.O.; Kurskiev, G.S.; Larionova, M.M.; Melnik, A.D.; Minaev, V.B.; Mironov, M.I.; Miroshnikov, I.V. Ion temperature measurements in a tokamak using active neutral particle analyzers diagnostics. *Plasma Phys. Control. Fusion* **2020**, *62*, 125010. [CrossRef]
10. Tournianski, M.R.; Akers, R.J.; Carolan, P.G.; Keeling, D.L. Anisotropic fast neutral particle spectra in the MAST spherical tokamak. *Plasma Phys. Control. Fusion* **2005**, *47*, 671–684. [CrossRef]
11. Schneider, P.A.; Blank, H.; Geiger, B.; Mank, K.; Martinov, S.; Ryter, F.; Weiland, M.; Weller, A.; the ASDEX Upgrade Team. A new compact solid-state neutral particle analyser at ASDEX Upgrade: Setup and physics modeling. *Rev. Sci. Instum.* **2015**, *86*, 073508. [CrossRef]
12. Geiger, B.; Stagner, L.; Heidbrink, W.W.; Dux, R.; Fischer, R.; Fujiwara, Y.; Garcia, A.V.; Jacobsen, A.S.; Jansen van Vuuren, A.; Karpushov, A.N.; et al. Progress in modelling fast-ion D-alpha spectra and neutral particle analyzer fluxes using FIDASIM. *Plasma Phys. Control. Fusion* **2020**, *62*, 095017. [CrossRef]
13. Schneider, W.; Turnyanskiy, M.R.; Chernyshev, F.V.; Afanasyev, V.I.; Kick, M.; Richert, T. Comparison of the IOFFE neutral particle analyser with the Princeton analyser on the Mega Amp Spherical Tokamak. *Vacuum* **2008**, *83*, 752–7568. [CrossRef]
14. Isobe, M.; Sassao, M.; Iiduka, S.; Krasilnikov, A.V.; Murakami, S.; Mutoh, T.; Osakabe, M.; Sudo, S.; Kawahata, K.; Ohyabu, N.; et al. Charge exchange neutral particle analysis with natural diamond detectors on LHD heliotron. *Rev. Sci. Instrum.* **2001**, *72*, 611. [CrossRef]

15. Ozaki, T.; Goncharov, P.; Sudo, S.; Seki, T.; Veschev, E.; Lyon, J. Horizontal, vertical, and radial high-energy particle distribution measurement system in Large Helical Device. *Rev. Sci. Instrum.* **2006**, *77*, 10E917. [CrossRef]
16. Goncharov, P.R.; Ozaki, T.; Sudo, S.; Tamura, N.; Kalinina, D.V.; Tespel Group; LHD Experimental Group; Veshchev, E.A.; Sergeev, V.Y. Active Neutral Particle Diagnostics on LHD by Locally Enhanced Charge Exchange on an Impurity Pellet Ablation Cloud. *Fusion Sci. Technol.* **2006**, *50*, 222. [CrossRef]
17. Bannmann, S.; Bozhenkov, S.; Äkäslompolo, S.; Poloskei, P.; Schneider, W.; Ford, O.; Wolf, R.C. Feasibility of neutral particle analysis for fast-ion measurements at W7-X. *J. Instrum.* **2022**, *17*, P01034. [CrossRef]
18. Fontdecaba, J.M.; Petrov, S.Y.; Nesenevich, V.G.; Ros, A.; Chernyshev, F.V.; McCarthy, K.J.; Barcala, J.M. Upgrade of the neutral particle analyzers for the TJ-II stellarator. *Rev. Sci. Instrum.* **2014**, *85*, 11E803. [CrossRef]
19. Afanasyev, V.I.; Chernyshev, F.V.; Kislyakov, A.I.; Kozlovski, S.S.; Lyublin, B.V.; Mironov, M.I.; Melnik, A.D.; Nesenevich, V.G.; Petrov, M.P.; Petrov, S.Y. Neutral particle analysis on ITER: Present status and prospects. *Nucl. Instrum. Methods Phys. Res.* **2010**, *621*, 456–467. [CrossRef]
20. Afanasyev, V.I.; Chernyshev, F.V.; Kozlovsky, S.S.; Melnik, A.D.; Marinin, G.V.; Mironov, M.I.; Navolotsky, A.S.; Nesenevich, V.G.; Petrov, M.P.; Petrov, S.Y.; et al. Development of the NPA based diagnostic complex in ITER. *J. Instrum.* **2022**, *17*, C07001. [CrossRef]
21. Du, X.D.; Van Zeeland, M.A.; Heidbrink, W.W.; Stagner, L.; Wingen, A.; Lin, D.; Collins, C.S. Resolving the fast ion distribution from imaging neutral particle analyzer measurements. *Nucl. Fusion* **2020**, *60*, 112001. [CrossRef]
22. Gusev, V.K.; Aminov, R.M.; Berezutskiy, A.A.; Bulanin, V.V.; Chernyshev, F.V.; Chugunov, I.N.; Dech, A.V.; Dyachenko, V.V.; Ivanov, A.E.; Khitrov, S.A.; et al. Investigation of beam– and wave–plasma interactions in spherical tokamak Globus-M. *Nucl. Fusion* **2011**, *51*, 103019. [CrossRef]
23. Gusev, V.K.; Bakharev, N.N.; Ber, B.Y.; Bulanin, V.V.; Chernyshev, F.V.; Dyachenko, V.V.; Goncharov, P.R.; Gusakov, E.Z.; Iblyaminova, A.D.; Irzak, M.A.; et al. Globus-M plasma physics research for fusion application and compact neutron source development. *Plasma Phys. Control. Fusion* **2016**, *58*, 014032. [CrossRef]
24. Gusev, V.K.; Azizov, E.A.; Alekseev, A.B.; Arneman, A.F.; Bakharev, N.N.; Belyakov, V.A.; Bender, S.E.; Bondarchuk, E.N.; Bulanin, V.V.; Bykov, A.S.; et al. Globus-M results as the basis for a compact spherical tokamak with enhanced parameters Globus-M2. *Nucl. Fusion* **2013**, *53*, 093013. [CrossRef]
25. Minaev, V.B.; Gusev, V.K.; Sakharov, N.V.; Varfolomeev, V.I.; Bakharev, N.N.; Belyakov, V.A.; Bondarchuk, E.N.; Brunkov, P.N.; Chernyshev, F.V.; Davydenko, V.I.; et al. Spherical tokamak Globus-M2: Design, integration, construction. *Nucl. Fusion* **2017**, *57*, 066047. [CrossRef]
26. Bakharev, N.N.; Balachenkov, I.M.; Chernyshev, F.V.; Chugunov, I.N.; Dyachenko, V.V.; Gusev, V.K.; Iliasova, M.V.; Khilkevitch, E.M.; Khromov, N.A.; Kiselev, E.O.; et al. First Globus-M2 Results. *Plasma Phys. Rep.* **2020**, *46*, 675–682. [CrossRef]
27. Petrov, Y.V.; Petrov, Y.V.; Gusev, V.K.; Sakharov, N.V.; Minaev, V.B.; Varfolomeev, V.I.; Dyachenko, V.V.; Balachenkov, I.M.; Bakharev, N.N.; Bondarchuk, E.N.; et al. Overview of GLOBUS-M2 spherical tokamak results at the enhanced values of magnetic field and plasma current. *Nucl. Fusion* **2022**, *62*, 042009. [CrossRef]
28. Izvozchikov, A.B.; Petrov, M.P.; Petrov, S.Y.; Chernyshev, F.V.; Shystov, I.V. The Akord-12 multichannel analyzer for simultaneous recording of the energy spectra of hydrogen and deuterium atoms. *Sov. Phys.-Tech. Phys.* **1992**, *37*, 201.
29. Chernyshev, F.V.; Afanasyev, V.I.; Dech, A.V.; Kick, M.; Kislyakov, A.I.; Kozlovskii, S.S.; Kreter, A.; Mironov, M.I.; Petrov, M.P.; Petrov, S.Y. A Compact Neutral-Particle Analyzer for Plasma Diagnostics. *Instrum. Exp. Tech.* **2004**, *47*, 214–220. [CrossRef]
30. Bakharev, N.N.; Bakharev, N.N.; Balachenkov, I.M.; Chernyshev, F.V.; Gusev, V.K.; Kiselev, E.O.; Kurskiev, G.S.; Melnik, A.D.; Minaev, V.B.; Mironov, M.I.; et al. Measurement of the fast ion distribution using active NPA diagnostics at the Globus-M2 spherical tokamak. *Plasma Phys. Control. Fusion* **2021**, *63*, 125036. [CrossRef]
31. Kurskiev, G.S.; Tolstyakov, S.Y.; Berezutskiy, A.A.; Gusev, V.K.; Kochergin, M.M.; Minaev, V.B.; Mukhin, E.E.; Patrov, M.I.; Petrov, Y.V.; Sakharov, N.V.; et al. Thomson scattering diagnostics upgrade at the Globus-M tokamak. *Probl. At. Sci. Technol. Ser. Thermonucl. Fusion* **2012**, *35*, 81–88. Available online: http://vant.iterru.ru/vant_2012_2/7.pdf (accessed on 6 February 2023). (In Russian) [CrossRef]
32. Larionova, M.M.; Miroshnikov, I.V.; Gusev, V.K.; Minaev, V.B.; Patrov, M.I.; Petrov, Y.V.; Sakharov, N.V.; Schegolev, P.B.; Telnova, A.Y.; Bakharev, N.N. CXRS measurements of ion temperature profile in NBI shots of the Globus-M spherical tokamak. *J. Phys. Conf. Ser.* **2019**, *1400*, 077018. [CrossRef]
33. Tel'nova, A.Y.; Miroshnikov, I.V.; Mitrankova, M.M.; Bakharev, N.N.; Gusev, V.K.; Zhil'tsov, N.S.; Kiselev, E.O.; Kurskiev, G.S.; Minaev, V.B.; Petrov, Y.V.; et al. First Results of the Ion Heat Transport Studies in the Globus-M2 Spherical Tokamak. *Tech. Phys. Lett.* **2021**, *47*, 470–473. [CrossRef]
34. Tukhmeneva, E.A.; Tolstyakov, S.Y.; Kurskiev, G.S.; Gusev, V.K.; Minaev, V.B.; Petrov, Y.V.; Sakharov, N.V.; Telnova, A.Y.; Bakharev, N.N.; Shchegolev, P.B.; et al. Development of Zeff diagnostic system on the Globus-M (M2) tokamak and the first experimental results. *Plasma Sci. Technol.* **2019**, *21*, 105104. [CrossRef]
35. Tukhmeneva, E.A.; Bakharev, N.N.; Varfolomeev, V.I.; Gusev, V.K.; Zhiltsov, N.S.; Kiselev, E.O.; Kurskiev, G.S.; Minaev, V.B.; Petrov, Y.V.; Sakharov, N.V.; et al. Measurement of Radiation Losses and Effective Ion Charge on the Globus-M2 Tokamak. *Tech. Phys. Lett.* **2021**, *47*, 56–60. [CrossRef]

36. Iliasova, M.V.; Iliasova, M.V.; Shevelev, A.E.; Khilkevitch, E.M.; Bakharev, N.N.; Skrekel, O.M.; Minaev, V.B.; Doinikov, D.N.; Gin, D.B.; Gusev, V.K.; et al. Neutron diagnostic system at the Globus-M2 tokamak. *Nucl. Instrum. Methods Phys. Res.* **2022**, *1029*, 166425. [CrossRef]
37. Lao, L.L.; John, H.S.; Stambaugh, R.D.; Kellman, A.G.; Pfeiffer, W. Reconstruction of current profile parameters and plasma shapes in tokamaks. *Nucl. Fusion* **1985**, *25*, 1611. [CrossRef]
38. Pankin, A.; McCune, D.; Andre, R.; Bateman, G.; Kritz, A. The tokamak Monte Carlo fast ion module NUBEAM in the National Transport Code Collaboration library. *Comp. Phys. Commun.* **2004**, *159*, 157–184. [CrossRef]
39. Chernyshev, F.V.; Afanasyev, V.I.; Gusev, V.K.; Ivanov, A.E.; Kurskiev, G.S.; Melnik, A.D.; Minaev, V.B.; Mironov, M.I.; Nesenevich, V.G.; Patrov, M.I.; et al. Study of fast-ion losses in experiments on neutral beam injection on the Globus-M spherical tokamak. *Plasma Phys. Rep.* **2011**, *37*, 553. [CrossRef]
40. Goncharov, P.R.; Kuteev, B.V.; Ozaki, T.; Sudo, S. Analytical and semianalytical solutions to the kinetic equation with Coulomb collision term and a monoenergetic source function. *Phys. Plasmas* **2010**, *17*, 112313. [CrossRef]
41. Chernyshev, F.V.; Ayushin, B.B.; Gusev, V.K.; D'yachenko, V.V.; Minaev, V.B.; Mironov, M.I.; Petrov, M.P.; Petrov, Y.V.; Sakharov, N.V.; Khitrov, S.A.; et al. Particle Diagnostics of Ion Cyclotron Resonance Plasma Heating in the Globus-M Tokamak. *Plasma Phys. Rep.* **2009**, *35*, 903–911. [CrossRef]
42. Kurskiev, G.S.; Miroshnikov, I.V.; Sakharov, N.V.; Gusev, V.K.; Petrov, Y.V.; Minaev, V.B.; Balachenkov, I.M.; Bakharev, N.N.; Chernyshev, F.V.; Goryainov, V.Y.; et al. The first observation of the hot ion mode at the Globus-M2 spherical tokamak. *Nucl. Fusion* **2022**, *62*, 104002. [CrossRef]
43. Mironov, M.I.; Chernyshev, F.V.; Afanasyev, V.I.; Melnik, A.D.; Navolotsky, A.S.; Nesenevich, V.G.; Petrov, M.P.; Petrov, S.Y. DOUBLE-MC Code: Modeling of Neutral Fluxes from Plasma. *Plasma Phys. Rep.* **2021**, *47*, 18–27. [CrossRef]
44. Fielding, S.J.; Axon, K.B.; Carolan, P.G.; Chernyshev, F.V.; Dunstan, M.; Durst, R.; Esser, H.G.; Edlington, T.; Hanks, S.D.; Jenkins, I.; et al. Boronization, recycling and isotope ratio control experiments on COMPASS. In Proceedings of the 18th Europhysics Conference, Geneva, Switzerland, 25 July–1 August 1991; Volume 15, pp. 73–76.
45. Bakharev, N.N.; Chernyshev, F.V.; Goncharov, P.R.; Gusev, V.K.; Iblyaminova, A.D.; Kornev, V.A.; Kurskiev, G.S.; Melnik, A.D.; Minaev, V.B.; Mironov, M.I.; et al. Fast particle behaviour in the Globus-M spherical tokamak. *Nucl. Fusion* **2015**, *55*, 043023. [CrossRef]
46. Gusev, V.K.; Bakharev, N.N.; Belyakov, V.A.; Ber, B.Y.; Bondarchuk, E.N.; Bulanin, V.V.; Bykov, A.S.; Chernyshev, F.V.; Demina, E.V.; Dyachenko, V.V.; et al. Review of Globus-M spherical tokamak results. *Nucl. Fusion* **2015**, *55*, 104016. [CrossRef]